



Improving the calibration-free complementary evaporation principle by linking with the Budyko framework

Daeha Kim¹, Minha Choi², Jong Ahn Chun³

¹Department of Civil Engineering, Jeonbuk National University, Jeonju, Jeollabuk-do, 54896, South Korea

5 ²Department of Water Resources, Sungkyunkwan University, Suwon, Gyeonggi-do, 16419, South Korea

³Prediction Research Department, APEC Climate Center, Busan, 48058, South Korea

Correspondence to: Jong Ahn Chun (jachun@apcc21.org)

Abstract. While it has performed well in predicting terrestrial evapotranspiration (ET_a) in many gauged locations over the world, the calibration-free complementary relationship (CR) depends on a questionable assumption that the Priestley-Taylor coefficient (α_e) is spatially constant over an extensive area. In this work, we evaluated the predictive performance of this convenient method, which only requires atmospheric inputs, against in-situ flux observations and water balance estimates (ET_{wb}) in Australia. We found that the CR method with a spatially constant α_e derived from fractional wet areas did not perform as highly as previous studies would suggest, underperforming three advanced ET_a models in closing basin-scale water balance. This problem was remedied by linking the CR method with a traditional Budyko equation that allowed upscaling of optimal α_e values from gauged basins to ungauged locations. The CR method with the α_e upscaled by the atmospheric inputs and the mean precipitation (P) better reproduced the grid ET_{wb} available over the entire continent, and outperformed the three ET_a models. This study suggests that the fixed α_e could lead the CR method to biased ET_a estimates, and it needs to be constrained by climate conditions to better close local water budgets.

20 1 Introduction

Evapotranspiration (ET_a) links water and energy exchanges between lands and the atmosphere. On the global scale, more than 60% of terrestrial precipitation (P) returns to the atmosphere through plants' vascular systems and soil pores, while consuming over 70% of surface net radiation (Trenberth et al., 2009; 2007). Since it is tightly coupled with carbon cycles, abnormally low ET_a indicates food insecurity and low ecosystem sustainability (Pareek et al., 2020; Kyatengerwa et al., 2020; Jasechko, 2018; Swann et al., 2016). In severe cases, ET_a limited by soil moisture can lead to extreme heatwaves that further propagate the water deficit in space and time (Schumacher et al., 2022; Miralles et al., 2014; Mueller and Seneviratne, 2012).

Despite great community efforts for sharing in-situ observations (e.g., Baldocchi, 2020; Novick et al., 2018), gauging networks for ET_a are still unevenly established over the world and often subject to limited data lengths (Ma et al., 2021). Unavoidably, modeling approaches are needed to predict ET_a in ungauged or poorly gauged locations, or to



characterize it at larger spatial and longer temporal scales. A wide range of modeling frameworks have been proposed such as physical models (e.g., Martens et al., 2017; Zhang et al., 2016), machine-learning techniques (e.g., Jung et al., 2019; Tramontana et al., 2016), and conceptual land surface schemes (e.g., Guimberteau et al., 2018; Haverd et al., 2018).

35 However, most of the ET_a models require P data and/or land surface information (e.g., remote-sensing vegetation indices) as major inputs. Owing to high uncertainty associated with P data (Sun et al., 2018) and model structure and parameterization (Zhang et al., 2019; Samaniego et al., 2017), ET_a models have produced substantial disparity in their estimates. In the comprehensive intercomparison by Pan et al. (2020), for example, the spread of the global mean ET_a simulated by 14 land surface schemes was larger than 200 mm a^{-1} , and similar incongruity between modeled ET_a estimates had found in the earlier Global Soil Wetness Project (Schlosser and Gao, 2010). This suggests a necessity of an alternative
40 method to circumvent the use of P and synthesized soil moisture.

A practical method to simulate ET_a without P and land-surface information is the complementary relationship (CR) of evaporation (Bouchet, 1963). It uses the evident fact that the air over a water-limited surface amplifies its vapor pressure deficit (VPD), while this effect disappears when the same surface is amply wet (Zhou et al., 2019; Chen and Buchberger, 2018; Ramírez et al., 2005). This atmospheric self-adjustment could become a predictor of water-limited ET_a , and various
45 methods have been formulated (e.g., Anayah and Kaluarachchi, 2014; Crago and Qualls, 2013; Huntington et al., 2011; Kahler and Brutsaert, 2006; Crago and Crowley, 2005; and Hobbins et al., 2004 among others). In particular, the non-dimensional derivation of Brutsaert (2015) and following modifications (Crago and Qualls, 2021; Szilagyi, 2021; Szilagyi et al., 2017; Crago et al., 2016) provided the generality and thermodynamic foundations of Bouchet's (1963) principle.

The non-dimensional CRs derived from definitive boundary conditions have showed outstanding performance in
50 reproducing ET_a observations at local, regional, and global scales (e.g., Ma et al., 2021; Brutsaert et al., 2020; Ma and Szilagyi, 2019; Ma et al., 2019; Crago and Qualls, 2018; Brutsaert et al., 2017), and their applications have extended to drought risk assessments (e.g., Kim et al., 2021; Kyatengerwa et al., 2020; Kim et al., 2019). However, to date, the only formulation that purely requires meteorological data and thus usable in ungauged areas is the one by Szilagyi et al. (2017). The other kindred methods depend on any reference ET_a data (e.g., eddy-covariance flux data or water-balance estimates) to
55 calibrate associated parameters that determine the hypothetical wet-environment evapotranspiration (ET_w). To resolve this problem, Szilagyi et al. (2017) analytically estimated the Priestley-Taylor coefficients (α_e) in wet locations only using atmospheric observations, and transferred their average value to the entire area of interest. This convenient calibration-free approach had well closed basin-scale water balance in the conterminous U.S. (Ma and Szilagyi, 2019), China (Ma et al., 2019), and 52 major river basins over the world (Ma et al., 2021).

60 Nonetheless, it seems to be an oversimplification to assume that α_e is constant over a large continental area. On many open-water surfaces, α_e has varied substantially on sub-daily, daily, monthly, and annual timescales (Han et al., 2021; Assouline et al., 2016; Baldocchi et al., 2016; Wang et al., 2014; Parlange and Katul, 1992). Given the space-time links between climate, soil, and vegetation (Hagedorn et al., 2019; Mekonnen et al., 2019; Rodriguez-Iturbe, 2000), the aerodynamic component of ET_w may not be described simply by a fixed fraction of the surface net radiation. The constant α_e



65 assumption might be unable to close surface energy balance under diverse climate and surface conditions, because the
 aerodynamic resistance plays a pivotal role in modulating surface temperature (Chen et al., 2020).

In this work, we proposed how to mend the problematic assumption of constant α_e in the Australian continent,
 where performance of the calibration-free CR has not yet thoroughly evaluated. By linking the CR and a traditional Budyko
 framework, here we analytically addressed why α_e cannot be fully independent of local climate conditions, and how it can be
 70 upscaled from gauged to ungauged locations while being constrained by local climate conditions.

2 Methodology and data

2.1 Calibration-free CR formulation by Szilagyi et al. (2017)

The CR of Szilagyi et al. (2017) describes the self-adjustment of ET_p to surface moisture conditions using three evaporation
 rates, namely, ET_a , ET_w , and the atmospheric evaporative potential (ET_p). Again, ET_a is the actual moisture flux from a land
 75 surface to the atmosphere, and ET_w is the hypothetical ET_a rate that should occur with ample water availability. ET_p is the
 atmospheric capacity to receive water vapor that responds actively to soil moisture conditions. By defining the two
 dimensionless variables as $x \equiv ET_w/ET_p$ and $y \equiv ET_a/ET_p$, and a definitive relationship between x and y could be derived
 from four boundary conditions.

Under ample water conditions, ET_p does not deviate from ET_w and ET_a (i.e., $ET_p = ET_w = ET_a$); hence, the
 80 corresponding zero-order boundary condition is (i) $y = 1$ for $x = 1$. In contrast, ET_a must be nil over a desiccated surface (i.e.,
 $y = 0$), and by energy balance, the surface net radiation should be fully transformed to the sensible heat flux. Then, the
 atmospheric VPD would be amplified at the maximum level under the given radiative forcing. Defining the maximum ET_p
 rate as E_{pmax} , another zero-order boundary condition is given as (ii) $y = 0$ for $x = x_{min} \equiv ET_w/E_{pmax}$. When $x = 1$ (i.e., ample
 water conditions), changes in ET_a would be controlled by changes in ET_w , yielding a first-order boundary condition as: (iii)
 85 $dy/dx = 1$ for $x = 1$. Over a desiccated surface, the zero ET_a cannot change irrespective of changes in ET_w and ET_p ; thus,
 another first-order boundary condition becomes (iv) $dy/dx = 0$ for $x = 0$. The simplest polynomial equation satisfying the
 four boundary conditions is:

$$y = 2X^2 - X^3, \quad (1a)$$

where, X rescales the dimensionless x into $[0, 1]$ as:

$$90 \quad X = \frac{x - x_{min}}{1 - x_{min}} = \frac{E_{pmax} - ET_p}{E_{pmax} - ET_w} \frac{ET_w}{ET_p}. \quad (1b)$$

Eq. (1) allows users to estimate ET_a with no land-surface information, because ET_p , ET_w , and E_{pmax} are all
 obtainable from a set of net radiation, air temperature, dew-point temperature, and wind speed data. ET_p and E_{pmax} could be
 estimated by the Penman (1948) equation:

$$ET_p = \frac{\Delta(T_a) R_n}{\Delta(T_a) + \gamma \lambda_v} + \frac{\gamma}{\Delta(T_a) + \gamma} f_u VPD, \quad (2)$$



$$95 \quad E_{pmax} = \frac{\Delta(T_{dry})}{\Delta(T_{dry}) + \gamma} \frac{R_n}{\lambda_v} + \frac{\gamma}{\Delta(T_{dry}) + \gamma} f_u e_s(T_{dry}), \quad (3)$$

where, $\Delta(T)$ is the slope of the saturation vapor pressure curve ($\text{kPa } ^\circ\text{C}^{-1}$) at a temperature T , T_a is the mean air temperature ($^\circ\text{C}$), γ is the psychrometric constant ($\text{kPa } ^\circ\text{C}^{-1}$), R_n is the surface net radiation less the soil heat flux ($\text{MJ m}^{-2} \text{d}^{-1}$), λ_v is the latent heat of vaporization (MJ kg^{-1}), $f_u = 2.6 (1 + 0.54 u_2)$ is the Rome wind function ($\text{mm d}^{-1} \text{kPa}^{-1}$), where u_2 is the 2-m wind speed (m s^{-1}), and VPD is $e_s(T_a)$ minus $e_s(T_{dew})$, where $e_s(T)$ is the saturation vapor pressure at T and T_{dew} is the dew point temperature ($^\circ\text{C}$).

T_{dry} in Eq. (3) is the air temperature ($^\circ\text{C}$) at which the boundary layer is devoid of humidity by the adiabatic drying process:

$$T_{dry} = T_{wb} + \frac{e_s(T_{wb})}{\gamma} = T_a + \frac{e_s(T_{dew})}{\gamma}, \quad (4)$$

where, T_{wb} is the wet-bulb temperature ($^\circ\text{C}$), where the saturation vapor pressure curve intersects with the adiabatic wetting line:

$$\gamma \frac{T_{wb} - T_{avg}}{e_s(T_{wb}) - e_a} = -1. \quad (5)$$

To quantify ET_w , the Priestly and Taylor (1972) equation has been a typical choice (e.g., Han and Tian, 2018; Szilagyi et al., 2017; Crago et al., 2016; Brutsaert, 2015):

$$ET_w = \alpha_e \frac{\Delta(T_w)}{\Delta(T_w) + \gamma} \frac{R_n}{\lambda_v}, \quad (6)$$

where, α_e varies usually within [1.10, 1.32] (Szilagyi et al., 2017), and T_w is the wet-environment air temperature ($^\circ\text{C}$). T_w can be approximated with the wet-surface temperature (T_{ws}), because negligible vertical air temperature gradient is observable in wet environments. Given the independence of T_{ws} on areal extent (Szilagyi and Schepers, 2014), it is obtainable by iteration from the Bowen ratio (β) of a small wet patch:

$$\beta = \frac{R_n - ET_p}{ET_p} \approx \gamma \frac{T_{ws} - T_a}{e_s(T_{ws}) - e_s(T_{dew})}. \quad (7)$$

The approximate Eq. (7) assumes that the available radiation for the wet patch is close to that of the drying surface (Szilagyi et al., 2017). T_{ws} might be higher than T_a when the air close to saturation. In such a case, T_{ws} needs to be constrained by T_a when estimating ET_w .

The single parameter for the non-dimensional CR, i.e., α_e , could be analytically obtained by inserting the Priestley-Taylor equation into the Bowen ratio of a wet environment (Szilagyi et al., 2017):

$$120 \quad \alpha_e = \frac{[\Delta(T_a) + \gamma][e_s(T_{ws}) - e_s(T_{dew})]}{\Delta(T_a)[e_s(T_{ws}) - e_s(T_{dew})] + \gamma[T_{ws} - T_a]}, \quad (8)$$

where, α_e must fall within the theoretical limit of $[1, 1 + \gamma/\Delta(T_a)]$ (Priestley and Taylor, 1972).

2.2 Data used for ET_a estimation and performance evaluation

Since Eq. (8) is applicable only in a wet environment, Szilagyi et al. (2017) identified wet locations in a continental area using the fact that the air close to saturation is likely to have high relative humidity (RH) and T_{ws} higher than T_a . Thus, α_e



125 values were calculated at locations with $RH > 90\%$ and $T_{ws} > T_a + 2\text{ }^\circ\text{C}$, and their average was assumed to be an unbiased α_e for every location of interest.

However, the spatially constant α_e may not be suitable in a continental area, because the dynamic equilibrium between the atmosphere and the underlying surface is intertwined with partitioning of P into ET_a and runoff (Q). Kim and Chun (2021) analytically linked Eq. (1) with the Turc-Mezentsev equation, and explained the variation of x with climatological aridity and an implicit land-surface parameter. To satisfy the underpinning independence between P and R_n , they reformulated the traditional Budyko equation with $\Phi_0 \equiv ET_w/P$ in lieu of the commonly used aridity index (i.e., $\Phi \equiv ET_p/P$) as:

$$\frac{ET_a}{P} = \frac{ET_w}{P} \left[\frac{1}{1 + \left(\frac{ET_w}{P}\right)^n} \right]^{\frac{1}{n}} = \frac{xET_p}{P} \left[\frac{1}{1 + \left(\frac{xET_p}{P}\right)^n} \right]^{\frac{1}{n}}, \quad (9)$$

where, n is the land-surface parameter that accounts for factors other than climatic controls affecting the partitioning of P . By dividing Eq. (9) with Φ , it is found that the P partitioning is intertwined with the dimensionless CR as:

$$135 \quad y = \frac{ET_a}{ET_p} = 2X^2 - X^3 = \left[\frac{x^n}{1 + x^n \Phi^n} \right]^{\frac{1}{n}}. \quad (10)$$

Eq. (10) implicates that the CR needs to be constrained by climatological aridity and surface properties.

When ET_a and P data are available at a sufficient number of river basins, Eq. (10) enables users to estimate x and n . Considering $x_{min} = xET_p/E_{pmax}$, the non-linear Eq. (10) could be simplified by x values from Eq. (10) and corresponding Φ , ET_p/E_{pmax} , and n as:

$$140 \quad \hat{x} = b_0 + b_1 \ln(\Phi) + b_2 \ln(ET_p/E_{pmax}) + b_2 \ln(n), \quad (11)$$

where, \hat{x} is the climatologically unbiased ratio of ET_w to ET_p , and b_0 , b_1 , and b_2 are the intercept and the regression coefficients, respectively. For ungauged locations where n is unavailable, Eq. (11) could be further approximated only using the climatic variables:

$$\hat{x} = c_0 + c_1 \ln(\Phi) + c_2 \ln(ET_p/E_{pmax}), \quad (12)$$

145 where, c_0 , c_1 , and c_2 are the intercept and the regression coefficients of the approximated equation. Using \hat{x} from Eq. (12), one could estimate α_e in an ungauged location as:

$$\hat{\alpha}_e = \hat{x} \frac{ET_p}{ET_{eq}} \quad (13a)$$

$$ET_{eq} = \frac{\Delta(T_w)}{\Delta(T_w) + \gamma} \frac{R_n}{\lambda_v} \quad (13b)$$

where, the estimated $\hat{\alpha}_e$ approximately satisfies the CR and the Budyko equation together, and ET_{eq} is the equilibrium evapotranspiration (mm d^{-1}). Note that P , ET_p , E_{pmax} , and ET_{eq} within Eqs. (9)-(13) must be on a timescale where the Turc-Mezentsev equation is valid (typically longer than a year), and $\hat{\alpha}_e$ should be bounded with the theoretical limits of $[1, 1 + \gamma/\Delta(T_a)]$.



2.3 Atmospheric forcing, eddy-covariance, and runoff datasets for application

We examined the CR combined with the Budyko framework in Australia lying within [10°- 45° S, 113°- 155° E]. The atmospheric forcing data (R_n , T_a , T_{dew} , and u_2) were collected from the advanced ERA5-Land reanalysis archive (Muñoz-Sabater et al., 2021) of the European Centre for Medium-Range Weather Forecasts (<https://cds.climate.copernicus.eu>; last access on Dec-10/2021). The monthly averages of surface latent and sensible heat fluxes, 2-m air temperature, 2-m dew-point temperature, and 10-m U and V wind speed components at $0.1^\circ \times 0.1^\circ$ were downloaded for 1981-2020. R_n was calculated by summing the two heat fluxes, and the 10-m wind speed components were converted to u_2 using the logarithmic vertical profile (Allen et al., 1998).

As a point-scale evaluation reference, monthly latent heat flux observations at the 16 eddy-covariance stations in Table 1 were taken from the FLUXNET2015 archive (<https://fluxnet.org/>; last access on Jul-1/2021). We chose the flux towers at which 24 or more monthly data with high quality ('LE_F_MDS_QC' > 0.95), and employed the latent heat flux data multiplied by the energy balance closure correction factor. Considering the fine resolution of the ERA5-Land forcing data, we believed that the resulting CR ET_a estimates could be compared directly with the point-scale observations.

As a basin-scale evaluation reference, we also collected the Australian edition of the Catchment Attributes and Meteorology for Large sample Studies (CAMELS; Fowler et al., 2021) series of datasets (available at <https://doi.org/10.1594/PANGAEA.921850>; last access on Sep-27/2021). The CAMELS datasets comprise daily time series of 19 hydrometeorological variables at 222 unregulated river basins in Australia. We took P and runoff (Q) data for 1981-2014 in 71 river basins larger than 500 km² that could contain at least five CR ET_a estimates at $0.1^\circ \times 0.1^\circ$. The basin-scale water balance was approximated by $ET_{wb} \approx \Sigma P - \Sigma Q$, where ET_{wb} is water-balance ET_a at the mean annual scale.

In addition, the SILO P data at $0.01^\circ \times 0.01^\circ$ were collected from the Queensland government (<https://www.longpaddock.qld.gov.au/silo/gridded-data>; last access on Jun-01/2021) together with the Global RUNoff (GRUN) ENSEMBLE data (Ghiggi et al., 2021) (<https://doi.org/10.6084/m9.figshare.12794075>; last access on Oct-1/2021). The global Q data were produced at $0.5^\circ \times 0.5^\circ$ using a machine-learning algorithm trained by in-situ streamflow observations, and potential errors were reduced by simulations with 21 different sets of atmospheric forcing (Ghiggi et al., 2021). After bilinearly unifying the resolutions of SILO P and GRUN Q datasets, we calculated the mean annual ET_{wb} for 1981-2016 at $0.5^\circ \times 0.5^\circ$ over the entire Australian continent.

Against the grid-scale ET_{wb} estimates, predictive performance of the CR method was compared with three ET_a products from a physical, a machine-learning, and a land-surface models. The physical model was the Global Land Evaporation Amsterdam Model (GLEAM) v3.2 (Martens et al., 2017; <https://www.gleam.eu>; last access on Jun-03/2020) based on the Priestley-Taylor equation constrained by microwave-derived soil moisture, surface temperature, and vegetation optical depth. The machine-learning ET_a product was the FluxCom (<http://www.fluxcom.org/>; last access Mar-18/2019) that upscaled in-situ observations at 224 eddy-covariance towers using 11 algorithms (Jung et al., 2019). Among the variations of the FluxCom products, we chose the one forced by the CRUNCEPv8 that has the longest data length from 1950 to 2016. The



land-surface-model-based product was the ERA5-Land monthly ET_a (<https://cds.climate.copernicus.eu>; last access on Jul-7/2021) simulated by the advanced Hydrology Tiled ECMWF Scheme for Surface Exchanges over Land scheme (Balsamo et al., 2015). We bilinearly unified the different resolutions of the modeled ET_a products to $0.5^\circ \times 0.5^\circ$, and their common period of the modeled ET_a products was 1981-2016.

190 3 Results

3.1 Performance of the calibration-free CR in Australia

Figure 1a depicts the spatial distribution of the inverse of aridity index ($\Phi^{-1} = P/ET_p$) that has been traditionally used for climate classification. The mean ratio between SILO P and ET_p for 1981-2014 shows that 81% of the Australian land surfaces were under arid ($\Phi^{-1} < 0.2$) and semi-arid climates ($0.2 < \Phi^{-1} < 0.5$). Semi-humid ($0.5 < \Phi^{-1} < 0.65$) and humid climates ($\Phi^{-1} > 0.65$) were only found in the northern and southeastern coastal areas and the southwestern edge where major cities and agricultural lands have developed. The blue-colored areas in Figure 1a are the locations with $RH > 90\%$ and $T_{ws} > T_a + 2^\circ C$, at which the α_e values from Eq. (8) were within 1.15 ± 0.064 (median \pm interquartile range). Though the two conditions were satisfied in some mountainous areas in the southeastern part, we excluded them because unexpectedly high α_e values were obtained. The median $\alpha_e = 1.15$ fell within the theoretically acceptable range, and was close to the values
200 found by Ma et al. (2019) and Ma and Szilagyi (2019).

Using $\alpha_e = 1.15$, we synthesized CR ET_a over the entire Australian continent (Figure 1b). The distribution of the mean CR ET_a for 1981-2014 was coherent with that of Φ^{-1} . The mean CR ET_a ranged in $248 \pm 99.7 \text{ mm a}^{-1}$ and $547 \pm 252 \text{ mm a}^{-1}$ under arid ($0.05 < \Phi^{-1} < 0.25$) and semi-arid ($0.25 < \Phi^{-1} < 0.50$) climates, respectively. In contrast, CR ET_a in semi-humid ($0.5 < \Phi^{-1} < 0.65$) and humid ($\Phi^{-1} > 0.65$) locations were much higher, being within $913 \pm 293 \text{ mm a}^{-1}$ and $960 \pm 333 \text{ mm a}^{-1}$, respectively. Hyper-arid climates ($\Phi^{-1} < 0.05$) were not found in Australia. The continental mean CR ET_a was 486.8 mm a^{-1} for 1981-2012, was about 10% higher than the estimate (439 mm a^{-1}) in Zhang et al.'s (2016) global-scale synthesis. The continental average of SILO P for 1981-2014 (473.2 mm a^{-1}) was slightly smaller than the mean CR ET_a , implicating that the calibration-free CR is likely to overrate ET_a .

The overestimation of the CR method was confirmed by comparing the ET_a estimates with the flux observations and the basin-scale ET_{wb} (Figure 2). The percent bias (p-bias) of the ET_a estimates were positive to the two observation sets. The regression slopes between estimated and observed ET_a were below 0.75, tending to overrate ET_a increasingly as climate becomes wetter. Despite the high Pearson correlation coefficient (Pearson r), the Nash-Sutcliffe efficiency (NSE) and the root mean square error (RMSE) between CR ET_a and ET_{wb} in the CAMELS basins indicated that the calibration-free CR did not perform as highly as in prior studies (Ma et al., 2021, Ma and Szilagyi, 2019; Ma et al., 2019; Kim et al., 2019).



215 One may argue that the median $\alpha_e = 1.15$ from the small fractional areas is unlikely representative of the entire Australian continent. Thus, we re-simulated ET_a using the global estimate of $\alpha_e = 1.10$ recently found by Ma et al. (2021). Though the performance measures were improved, the overestimating tendency did not disappear (Figure 3).

3.2 The empirical relationship between \hat{x} to climatic variables

220 Figures 2 and 3 imply that the calibration-free CR with a fixed α_e was unlikely good at closing local water balance particularly in (semi-)humid river basins. To find climatologically unbiased α_e , we first estimated the climatological x and the parameter n of the CAMLES basins using Eq. (10) using the averages of ET_{wb} , P , ET_p , and E_{pmax} over 1981-2014. Figure 4a-c shows the scatter plots between the resultant x and corresponding Φ , ET_p/E_{pmax} , and n values. The Pearson r between the x and the other three variables was -0.83, -0.49, and 0.44, respectively (significant at 1% level), suggesting that the self-adjustment of ET_p is affected not only by climate conditions, but by land surface properties at least in part.

225 By regressing the x values with log-transformed Φ , ET_p/E_{pmax} and n , we obtained an empirical relationship that enables to estimate the climatological ratio of ET_w to ET_p as:

$$\hat{x} = 0.964 - 0.206 \ln(\Phi) + 0.261 \ln(ET_p/E_{pmax}) + 0.0750 \ln(n). \quad (14)$$

The regression coefficients were all significant at 1% level, and the coefficient of determination (R^2) was 0.98. The regression equation was further approximated by discarding n from the explanatory variables:

230
$$\hat{x} = 1.047 - 0.221 \ln(\Phi) + 0.251 \ln(ET_p/E_{pmax}). \quad (15)$$

The R^2 of the approximated Eq. (15) declined to 0.88. We also found that the simple regression between x and Φ provided the R^2 of 0.84. In other words, though the spatial variation of x could be explained mostly by changes in climatological aridity, heterogeneous land properties might exert non-negligible influences. About 10% of predictability was lost by neglecting the implicit effect of land properties on changes in \hat{x} .

235 Despite the decreased R^2 , the approximated Eq. (15) performed acceptably in reproducing the x values directly from CR (Figure 4d). The NSE, RMSE, Pearson r , and p -bias between the predicted \hat{x} and the x from CR were 0.88, 0.03, 0.94, and 0.0%, respectively.

3.3 Evaluation of annual ET_a and decadal trends against grid-scale water balance

By multiplying \hat{x} to the climatological ratio between ET_p and ET_{eq} , we determined $\hat{\alpha}_e$ across the Australian land surfaces. Figure 5a illustrates the distribution of the resulting $\hat{\alpha}_e$ that varies within 1.08 ± 0.19 . The median α_e (1.08) was smaller than 240 the Ma et al.'s (2021) global-scale estimate (1.10). The $\hat{\alpha}_e$ values were relatively high in the northwestern and the northern part, whereas they were mostly below the median in the southern and the eastern parts. On 24% of the Australian land surfaces, $\hat{\alpha}_e$ values were unity, implying that they might be below the theoretical lower limit unless bounded.

We re-simulated CR ET_a using the spatially varying $\hat{\alpha}_e$, and found that the overestimating tendency was reduced 245 considerably (Figure 5b). Under arid and semi-arid climates, the mean CR ET_a ranged within $231 \pm 86.2 \text{ mm a}^{-1}$ and $507 \pm$



247 mm a⁻¹ for 1981-2014, while it decreased to 797 ± 406 mm a⁻¹ and 806 ± 410 mm a⁻¹ in semi-humid and humid regions, respectively. The continental mean ET_a for 1981-2012 declined to 441 mm a⁻¹, being practically equal to Zhang et al.'s (2016) estimate, and providing a physically plausible evaporative fraction (93% of P). As expected, the water-balance ET_{wb} in the CAMELS basins were better reproduced by employing the varying $\hat{\alpha}_e$ values, while keeping the point-scale
250 reproducibility at flux tower locations (Figure 6).

Since the empirical Eq. (15) was built by ET_{wb} of the CAMELS basins, one may argue that the evaluation against the same reference would be unfair. Hence, after resampling to 0.5°×0.5°, we compared the CR ET_a estimates against the grid ET_{wb} over the entire Australian continent together with the modeled ET_a by GLEAM, FluxCom, and ERA5-Land. As shown, the CR method with $\alpha_e = 1.15$ overrated the mean annual ET_a for 1981-2016 along the eastern and the northern
255 coastlines (Figure 7b), underperforming the physical, the machine-learning, and the land surface models (Figure 8a). Although the smaller constant $\alpha_e = 1.10$ made the CR method perform better, its predictability was still poorer than the three models and the variation of residuals seemed to be as large as in the simulations with $\alpha_e = 1.15$ (Figure 8b).

When employing the spatially varying $\hat{\alpha}_e$, on the other hand, the same CR formulation could alleviate overestimations along the coastlines (Figure 7c). The varying $\hat{\alpha}_e$ resulted in the CR ET_a estimates agreeing more neatly with
260 the grid ET_{wb}, and the variation of residuals was much smaller than in the case of $\alpha_e = 1.10$ (Figure 8c). The CR method with variable $\hat{\alpha}_e$ outperformed the advanced models in reproducing the grid ET_{wb} (Figure 8). Although the referenced ET_{wb} may have some errors associated with upscaling of P and Q observations to the grid scale, our comparative evaluation suggests that discarding the assumption of a fixed α_e could reduce the variation of errors considerably.

4 Discussion

265 4.1 Determination of α_e and the Budyko framework

In seven Australian eddy-covariance flux towers, Crago et al. (2022) found that the optimal α_e for the CR of Szilagyi et al. (2017) was 1.35 when predicting daily ET_a in the dimensionless form (i.e., $y = ET_a/ET_p$). However, it should be increased to 1.42, 1.45, 1.47, and 1.50 to simulate dimensional latent heat fluxes at daily, weekly, monthly, and annual timescales, respectively. In Crago and Qualls (2018), the optimal α_e for the kindred linear CR of Crago et al. (2016) varied between 1.00
270 and 1.43. The prior point-scale experiments have already suggested that a constant α_e is unlikely suitable for the non-dimensional CRs to predict ET_a in Australia.

Evidently, the ratio between the aerodynamic and the radiation components of the Penman equation is affected by the entrainment from the top of the boundary layer (Baldocchi et al., 2016), the dissimilarity between heat and water vapor sources (Assouline et al., 2016), the large-scale synoptic changes (Guo et al., 2015), the horizontal advection of dry air mass
275 (Jury and Tanner, 1975) and among others. More recently, Han et al. (2021) proved the non-linear dependence of ET_w on ET_{eq} using the sigmoid CR of Han and Tian (2018). Yang and Roderick (2019) empirically found that α_e varies with R_n even



over ocean surfaces. The theoretical and empirical evidence is counterintuitive to the constant α_e assumption underpinning the calibration-free CR.

280 Although Ma et al. (2021) highlighted the global applicability of the calibration-free CR, its performance was
remained unknown in most of the Australian land surfaces and in many ungauged basins over the world. Given the spatially
diverse climate conditions, assuming a single α_e value across the continental area is questionable. Here, we analytically
addressed that the dimensionless CR relates to the Budyko framework describing the long-term water balance simply with
the climatological aridity. The Turc-Mezentsev equation enables users to develop an empirical relationship between climate
(i.e., Φ and ET_p/E_{pmax}) and the degree of ET_p adjustment (i.e., \hat{x}), making the CR method better close local water budgets.
285 The comparative evaluation highlights that the α_e values constrained by diverse climate conditions is likely to make the CR
method outperform the advanced physical, machine-learning, and land surface models. Thus, neglecting local P data may not
be a good choice when predicting ET_a with the CR method in ungauged areas. It is noteworthy that Φ was the dominant
control of the \hat{x} variation.

While here we addressed the problematic assumption of spatially constant α_e , more questions could be raised when
290 employing the polynomial or a kindred CR. For example, the α_e values obtained from the Rome wind function would
inherently rely upon an unrealistic assumption that the aerodynamic resistance on a vegetated surface is equivalent to that of
open-water surfaces. However, it is unknown if this assumption is practically valid, because the Penman equation formulated
with the Rome wind function may result in unrealistically high ET_p even over large wet areas (McMahon et al., 2013). Given
the importance of the aerodynamic resistance in modulating surface temperature (Chen et al., 2020), ignoring its temporal
295 variability may become a considerable error source may affect the performance of the CR method sub-annual timescales.
Since the steady-state Budyko equation is unlikely to resolve this problem, further improvements are necessary for the CR
formulations.

4.2 Limitations

We employed the meteorological data different from those used in Ma et al. (2021). The ERA5-Land data are more advanced
300 and produced at a higher resolution than the ERA5 data (Hersbach et al., 2020) by which Ma et al. (2021) predicted ET_a
globally. Ma et al. (2021) incorporated remotely sensed albedo and emissivity together with a correction factor when
calculating R_n , whereas we directly employed the sum of the ERA5-Land latent and sensible heat fluxes. Those input
differences, too, may lead to discrepancy in CR ET_a estimates.

The gridded GRUN Q dataset also has some uncertainty sources, though it is the ensemble of many runoff
305 simulations from 21 different atmospheric forcing inputs. In the associated machine-learning process, some Q observations
affected by human activities (e.g., dam regulation and return flows from groundwater abstraction) might not be excluded,
potentially disrupting the empirical relationship between atmospheric forcing and natural flows (Ghiggi et al., 2021). In
addition, the uncertainty of SILO P might be non-negligible in areas with limited weather stations and in mountainous areas



(Fu et al., 2022). Though we reduced the potential errors in the gridded P and Q datasets by temporal averaging, the grid-
310 scale ET_{wb} estimates should be treated as plausible values rather than exact observations.

5 Conclusions

In this work, we showed the calibration-free CR is unlikely to perform well in Australia due at least to the assumption of a constant Priestley-Taylor coefficient. We resolved this problem by linking the CR with the traditional Turc-Mezentsev equation, and drew the following conclusions:

- 315 (1) The constant Priestley-Taylor coefficient transferred from fractional wet locations could lead the CR method to poor performance in closing basin-scale water balance. The CR with a constant Priestley-Taylor coefficient seemed to underperform the widely used physical, machine-learning, and land surface models.
- (2) The Budyko framework could provide an additional condition that constrains the degree of ET_p adjustment at the mean annual scale, upscaling the optimal Priestley-Taylor coefficients from gauged to ungauged locations.
- 320 (3) The Priestley-Taylor coefficients constrained by diverse climate conditions showed outstanding performance in closing the local water balance over the Australian continent, and the CR method outperformed the other advanced ET_a models.

Author contributions

325 DK, MC, and JAC organized this study together. DK built the research framework, simulated ET_a with the CR method, and drafted the manuscript. JAC processed the modeled ET_a datasets and reviewed the draft, and MC actively participated in discussion.

Competing interests

The authors declare no competing interests.

330 Code availability

The Python scripts that implement the CR method are available upon request from the leading author (daeha.kim@jbnu.ac.kr).



Acknowledgements

This study is supported by the APEC Climate Center. We also acknowledge the financial support of the National Research
335 Foundation of Korea (NRF) funded by the Korea government (MSIT) (NRF-2019R1A2B5B01070196).

References

- Allen, R. G., Pereira, L. S., Raes, D., and Smith, M.: Crop evapotranspiration - Guidelines for computing crop water requirements - FAO Irrigation and drainage paper 56, Food and Agriculture Organization of the United Nations, Rome, 1998.
- 340 Anayah, F. M., and Kaluarachchi, J. J.: Improving the complementary methods to estimate evapotranspiration under diverse climatic and physical conditions, *Hydrol. Earth Syst. Sci.*, 18, 2049–2064, <https://doi.org/10.5194/hess-18-2049-2014>, 2014.
- Assouline, S., Li, D., Tyler, S., Tanny, J., Cohen, S., Bou-Zeid, E., Parlange, M., and Katul, G. G.: On the variability of the Priestley-Taylor coefficient over water bodies, *Water Resour. Res.*, 52, 150–163, <https://doi.org/10.1002/2015wr017504>,
345 2016.
- Baldocchi, D., Knox, S., Dronova, I., Verfaillie, J., Oikawa, P., Sturtevant, C., Matthes, J. M., and Detto, M.: The impact of expanding flooded land area on the annual evaporation of rice, *Agric. Forest Meteorol.* 223, 181–193. <https://doi.org/10.1016/j.agrformet.2016.04.001>, 2016
- Baldocchi, D. D.: How eddy covariance flux measurements have contributed to our understanding of Global Change
350 Biology, *Glob. Change Biol.*, 26, 242–260, <https://doi.org/10.1111/gcb.14807>, 2020.
- Balsamo, G., Albergel, C., Beljaars, A., Boussetta, S., Brun, E., Cloke, H., Dee, D., Dutra, E., Muñoz-Sabater, J., Pappenberger, F., de Rosnay, P., Stockdale, T., and Vitart, F.: ERA-Interim/Land: a global land surface reanalysis data set, *Hydrol. Earth Syst. Sci.*, 19, 389–407. <https://doi.org/10.5194/hess-19-389-2015>, 2015.
- Bouchet, R. J.: Evapotranspiration réelle et potentielle, signification climatique, in: General Assembly Berkeley, Int. Assoc.
355 Sci. Hydrol., Gentbrugge, Belgium, Publ. No. 62, 134–142, 1963.
- Brutsaert, W., Li, W., Takahashi, A., Hiyama, T., Zhang, L., and Liu, W.: Nonlinear advection-aridity method for landscape evaporation and its application during the growing season in the southern Loess Plateau of the Yellow River basin, *Water Resour. Res.*, 53, 270–282. <https://doi.org/10.1002/2016WR019472>, 2017
- Brutsaert, W., Cheng, L., and Zhang, L.: Spatial distribution of global landscape evaporation in the early twenty-first century
360 by means of a generalized complementary approach, *J. Hydrometeorol.*, 21, 287–298, <https://doi.org/10.1175/JHM-D-19-0208.1>, 2020.
- Brutsaert, W.: A generalized complementary principle with physical constraints for land-surface evaporation, *Water Resour. Res.*, 51, 8087–8093, <https://doi.org/10.1002/2015WR017720>, 2015.



- Chen, X., and Buchberger, S. G.: Exploring the relationships between warm-season precipitation, potential evaporation, and
365 “apparent” potential evaporation at site scale, *Hydrol. Earth Syst. Sci.* 22, 4535–4545. <https://doi.org/10.5194/hess-22-4535-2018>, 2018.
- Chen, C., Li, D., Li, Y., Piao, S., Wang, X., Huang, M., Gentine, P., Nemani, R. R. and Myneni, R. B.: Biophysical impacts
of Earth greening largely controlled by aerodynamic resistance, *Sci. Adv.*, 6, eabb1981,
<https://doi.org/10.1126/sciadv.abb1981>, 2020.
- 370 Crago, R., and Crowley, R.: Complementary relationships for near-instantaneous evaporation, *J. Hydrol.*, 300(1-4), 199–211,
<https://doi.org/10.1016/j.jhydrol.2004.06.002>, 2005.
- Crago, R. D., and Qualls, R. J.: The value of intuitive concepts in evaporation research, *Water Resour. Res.*, 49, 6100–6104,
<https://doi.org/10.1002/wrcr.20420>, 2013.
- Crago, R. D., and Qualls, R. J.: Evaluation of the generalized and rescaled complementary evaporation relationships, *Water*
375 *Resour. Res.*, 54, 8086–8102, <https://doi.org/10.1029/2018WR023401>, 2018.
- Crago, R. D., and Qualls, R. J.: A graphical interpretation of the rescaled complementary relationship for evapotranspiration.
Water Resour. Res., 57, e2020WR028299. <https://doi.org/10.1029/2020WR028299>, 2021.
- Crago, R., Szilagyi, J., Qualls, R., and Huntington, J.: Rescaling the complementary relationship for land surface
evaporation, *Water Resour. Res.*, 52, 8461–8471, <https://doi.org/10.1002/2016WR019753>, 2016.
- 380 Crago, R. D., Qualls, R., and Szilagyi, J.: Complementary Relationship for evaporation performance at different spatial and
temporal scales, *J. Hydrol.*, 608, 127575, <https://doi.org/10.1016/j.jhydrol.2022.127575>, 2022.
- Fowler, K. J. A., Acharya, S. C., Addor, N., Chou, C., and Peel, M. C.: CAMELS-AUS: hydrometeorological time series and
landscape attributes for 222 catchments in Australia, *Earth Syst. Sci. Data*, 13, 3847–3867, <https://doi.org/10.5194/essd-13-3847-2021>, 2021.
- 385 Fu, G., Barron, O., Charles, S. P., Donn, M. J., Van Niel, T. G., and Hodgson, G.: Uncertainty of gridded precipitation at
local and continent scales: A direct comparison of rainfall from SILO and AWAP in Australia, *Asia-Pacific J. Atmos. Sci.*,
in press, <https://doi.org/10.1007/s13143-022-00267-4>, 2022.
- Ghiggi, G., Humphrey, V., Seneviratne, S. I., and Gudmundsson, L.: G-RUN ENSEMBLE: A multi-forcing observation-
based global runoff reanalysis, *Water Resour. Res.*, 57, e2020WR028787, <https://doi.org/10.1029/2020WR028787>, 2021.
- 390 Guimberteau, M., Zhu, D., Maignan, F., Huang, Y., Yue, C., Dantec-Nédélec, S., Ottlé, C., Jornet-Puig, A., Bastos, A.,
Laurent, P., Goll, D., Bowring, S., Chang, J., Guenet, B., Tifafi, M., Peng, S., Krinner, G., Ducharne, A., Wang, F., Wang,
T., Wang, X., Wang, Y., Yin, Z., Lauerwald, R., Joetzjer, E., Qiu, C., Kim, H., and Ciais, P.: ORCHIDEE-MICT (v8.4.1),
a land surface model for the high latitudes: model description and validation, *Geosci. Model Dev.*, 11, 121–163.
<https://doi.org/10.5194/gmd-11-121-2018>, 2018.
- 395 Guo, X., Liu, H., and Yang, K.: On the application of the Priestley–Taylor relation on sub-daily time scales, *Boundary Layer*
Meteorol., 156, 489–499, <https://doi.org/10.1007/s10546-015-0031-y>, 2015.



- Hagedorn, F., Gavazov, K., and Alexander, J. M.: Above- and belowground linkages shape responses of mountain vegetation to climate change, *Science*, 365, 1119-1123, <https://doi.org/10.1126/science.aax4737>, 2019.
- Han, S., and Tian, F.: Derivation of a sigmoid generalized complementary function for evaporation with physical constraints, *Water Resour. Res.*, 54, 5050–5068, <https://doi.org/10.1029/2017WR021755>, 2018.
- Han, S., Tian, F., Wang, W., and Wang, L.: Sigmoid generalized complementary equation for evaporation over wet surfaces: A nonlinear modification of the Priestley-Taylor equation, *Water Resour. Res.*, 57, e2020WR028737, <https://doi.org/10.1029/2020WR028737>, 2021.
- Haverd, V., Smith, B., Nieradzic, L., Briggs, P. R., Woodgate, W., Trudinger, C. M., Canadell, J. G., and Cuntz, M.: A new version of the CABLE land surface model (Subversion revision r4601) incorporating land use and land cover change, woody vegetation demography, and a novel optimisation-based approach to plant coordination of photosynthesis, *Geosci. Model Dev.*, 11, 2995–3026, <https://doi.org/10.5194/gmd-11-2995-2018>, 2018.
- Hersbach, H., Bell, B., Berrisford, P., Hirahara, S., Horányi, A., Muñoz-Sabater, J., Nicolas, J., Peubey, C., Radu, R., et al.: The ERA5 global reanalysis, *Q. J. R. Meteorol. Soc.* 146, 1999-2049. <http://doi.org/10.1002/qj.3803>, 2020.
- Hobbins, M. T., Ramírez, J. A., and Brown, T. C.: Trends in pan evaporation and actual evapotranspiration across the conterminous U.S.: Paradoxical or complementary? *Geophys. Res. Lett.*, 31, L13503, <https://doi.org/10.1029/2004GL019846>, 2004.
- Huntington, J. L., Szilagyi, J., Tyler, S. W., and Pohll, G. M.: Evaluating the complementary relationship for estimating evapotranspiration from arid shrublands, *Water Resour. Res.*, 47, W05533, <https://doi.org/10.1029/2010WR009874>, 2011.
- Jasechko, S.: Plants turn on the tap, *Nature Clim. Change*, 8, 562–563, <https://doi.org/10.1038/s41558-018-0212-z>, 2018.
- Jung, M., Koirala, S., Weber, U., Ichii, K., Gans, F., Camps-Valls, G., Papale, D., Schwalm, C., Tramontana, G., and Reichstein, M.: The FLUXCOM ensemble of global land-atmosphere energy fluxes. *Sci. data*, 6, 74, <https://doi.org/10.1038/s41597-019-0076-8>, 2019.
- Jury, W. and Tanner, C.: Advection modification of the Priestley and Taylor evapotranspiration formula, *Agron. J.*, 67, 840–842, <https://doi.org/10.2134/agronj1975.000219620>, 1975.
- Kahler, D. M., and Brutsaert, W.: Complementary relationship between daily evaporation in the environment and pan evaporation, *Water Resour. Res.*, 42, W05413, <https://doi.org/10.1029/2005WR004541>, 2006.
- Kim, D., and Chun, J. A.: Revisiting a two-parameter Budyko equation with the complementary evaporation principle for proper consideration of surface energy balance, *Water Resour. Res.*, 57, e2021WR030838, <https://doi.org/10.1029/2021WR030838>, 2021.
- Kim, D., Ha, K.-J., and Yeo, J.-H.: New drought projections over East Asia using evapotranspiration deficits from the CMIP6 warming scenarios, *Earths Future*, 9, e2020EF001697, <https://doi.org/10.1029/2020EF001697>, 2021.
- Kyatengerwa, C., Kim, D., and Choi, M.: A national-scale drought assessment in Uganda based on evapotranspiration deficits from the Bouchet hypothesis, *J. Hydrol.*, 500, 124348, <https://doi.org/10.1016/j.jhydrol.2019.124348>, 2020.



- 430 Ma, N., and Szilagyi, J.: The CR of evaporation: a calibration-free diagnostic and benchmarking tool for large-scale
terrestrial evapotranspiration modeling. *Water Resour. Res.*, 55, 7246–7274, <https://doi.org/10.1029/2019WR024867>,
2019.
- Ma, N., Szilagyi, J., Zhang, Y., and Liu, W.: Complementary-relationship-based modeling of terrestrial evapotranspiration
across China during 1982–2012: validations and spatiotemporal analyses, *J. Geophys. Res. Atmos.*, 124, 4326–4351,
435 <https://doi.org/10.1029/2018JD029850>, 2019.
- Ma, N., Szilagyi, J., and Zhang, Y.: Calibration-free complementary relationship estimates terrestrial evapotranspiration
globally, *Water Resour. Res.*, 57, e2021WR029691, <https://doi.org/10.1029/2021WR029691>, 2021.
- Martens, B., Schumacher, D. L., Wouters, H., Muñoz-Sabater, J., Verhoest, N. E. C., and Miralles, D. G.: Evaluating the
land-surface energy partitioning in ERA5, *Geosci. Model Dev.*, 13, 4159–4181, <https://doi.org/10.5194/gmd-13-4159->
440 2020, 2020.
- McMahon, T. A., Peel, M., Lowe, L., Srikanthan, R., and McVicar, T.: Estimating actual, potential, reference crop and pan
evaporation using standard meteorological data: A pragmatic synthesis, *Hydrol. Earth Syst. Sci.*, 17, 1331–1363,
<https://doi.org/10.5194/hess-17-1331-2013>, 2013.
- Mekonnen, Z. A., Riley, W. J., Randerson, J. T., Grant, R. F., and Rogers, B. M.: Expansion of high-latitude deciduous
445 forests driven by interactions between climate warming and fire, *Nature plants*, 5, 952–958,
<https://doi.org/10.1038/s41477-019-0495-8>, 2019.
- Miralles, D. G., Teuling, A., J. van Heerwaarden, C. C., and de Arellano, J. V.-G.: Mega-heatwave temperatures due to
combined soil desiccation and atmospheric heat accumulation, *Nature Geosci.*, 7, 345–349,
<https://doi.org/10.1038/ngeo2141>, 2014.
- 450 Mueller, B., and Seneviratne, S. I.: Hot days induced by precipitation deficits at the global scale, *P. Natl. Acad. Sci. USA*,
109, 12398–12403, <https://doi.org/10.1073/pnas.1204330109>, 2012.
- Muñoz-Sabater, J., Dutra, E., Agustí-Panareda, A., Albergel, C., Arduini, G., Balsamo, G., Boussetta, S., Choulga, M.,
Harrigan, S., Hersbach, H., Martens, B., Miralles, D. G., Piles, M., Rodríguez-Fernández, N. J., Zsoter, E., Buontempo, C.,
and Thépaut, J.-N.: ERA5-Land: a state-of-the-art global reanalysis dataset for land applications, *Earth Syst. Sci. Data*, 13,
455 4349–4383, <https://doi.org/10.5194/essd-13-4349-2021>, 2021.
- Novick, K. A., Biederman, J. A., Desai, A. R., Litvak, M. E., Moore, D. J. P., Scott, R. L., and Torn, M. S.: The AmeriFlux
network: A coalition of the willing, *Agric. Forest Meteorol.*, 249, 444–456, <https://doi.org/10.1016/j.agrformet.2017.10.00>,
2018.
- Pan, S., Pan, N., Tian, H., Friedlingstein, P., Sitch, S., Shi, H., Arora, V. K., Haverd, V., Jain, A. K., Kato, E., Lienert, S.,
460 Lombardozi, D., Nabel, J. E. M. S., Ottlé, C., Poulter, B., Zaehle, S., and Running, S. W.: Evaluation of global terrestrial
evapotranspiration using state-of-the-art approaches in remote sensing, machine learning and land surface modeling,
Hydrol. Earth Syst. Sci., 24, 1485–1509, <https://doi.org/10.5194/hess-24-1485-2020>, 2020.



- Pareek, A., Dhankher, O. P., and Foyer, C. H.: Mitigating the impact of climate change on plant productivity and ecosystem sustainability, *J. Exp. Bot.*, 71, 451–456, <https://doi.org/10.1093/jxb/erz518>, 2020.
- 465 Parlange, M. B., and Katul, G. G.: Estimation of the diurnal variation of potential evaporation from a wet bare soil surface, *J. Hydrol.*, 132, 71–89, [https://doi.org/10.1016/0022-1694\(92\)90173-s](https://doi.org/10.1016/0022-1694(92)90173-s), 1992.
- Penman, H. L.: Natural evaporation from open water, bares soil, and grass, *Proc. R. Soc. Lond., Ser. A*, 193, 120–146. <https://doi.org/10.1098/rspa.1948.0037>, 1948.
- Priestley, C. H., and Taylor, R. J.: On the assessment of surface heat flux and evaporation using large-scale parameters. *Mon. Weather Rev.*, 100, 81–92. [https://doi.org/10.1175/1520-0493\(1972\)100<0081:OTAOSH>2.3.CO;2](https://doi.org/10.1175/1520-0493(1972)100<0081:OTAOSH>2.3.CO;2), 1972.
- 470 Ramírez, J. A., Hobbins, M. T., and Brown, T. C.: Observational evidence of the complementary relationship in regional evaporation lends strong support for Bouchet's hypothesis, *Geophys. Res. Lett.*, 32, L15401, <https://doi.org/10.1029/2005GL023549>, 2005.
- Rodriguez-Iturbe, I.: Ecohydrology: A hydrologic perspective of climate-soil-vegetation dynamics, *Water Resour. Res.*, 36, 3–9, <https://doi.org/10.1029/1999WR900210>, 2000.
- 475 Samaniego, L., Kumar, R., Thober, S., Rakovec, O., Zink, M., Wanders, N., Eisner, S., Müller Schmied, H., Sutanudjaja, E. H., Warrach-Sagi, K., and Attinger, S.: Toward seamless hydrologic predictions across spatial scales, *Hydrol. Earth Syst. Sci.*, 21, 4323–4346, <https://doi.org/10.5194/hess-21-4323-2017>, 2017.
- Schlosser, C. A., and Gao, X.: Assessing evapotranspiration estimates from the second global soil wetness project (GSWP-2) simulations, *J. Hydrometeorol.*, 11, 880–897, <https://doi.org/10.1175/2010jhm1203.1>, 2010.
- 480 Schumacher, D.L., Keune, J., van Heerwaarden, C.C., de Alrellano, J. V., Teuling, A. J., and Miralles, D. G.: Amplification of mega-heatwaves through heat torrents fuelled by upwind drought, *Nat. Geosci.*, 12, 712–717, <https://doi.org/10.1038/s41561-019-0431-6>, 2019.
- Sun, Q., Miao, C., Duan, Q., Ashouri, H., Sorooshian, S., and Hsu, K.-L.: A review of global precipitation datasets: Data sources, estimation, and intercomparisons, *Rev. Geophys.*, 56, 79–107, <https://doi.org/10.1002/2017rg000574>, 2018.
- 485 Swann, A. L., Hoffman, F. M., Koven, C. D., and Randerson, J. T.: Plant responses to increasing CO₂ reduce estimates of climate impacts on drought severity, *P. Natl. Acad. Sci. USA*, 113, 10019–10024, <https://doi.org/10.1073/pnas.1604581113>, 2016.
- Szilagyi, J., and Schepers, A.: Coupled heat and vapor transport: The thermostat effect of a freely evaporating land surface, *Geophys. Res. Lett.*, 41, 435–441, <https://doi.org/10.1002/2013gl058979>, 2014.
- 490 Szilagyi, J., Crago, R., and Qualls, R.: A calibration-free formulation of the complementary relationship of evaporation for continental-scale hydrology, *J. Geophys. Res. Atmos.*, 122, 264–278, <https://doi.org/10.1002/2016jd025611>, 2017.
- Szilagyi, J.: On the thermodynamics foundations of the complementary relationship of evaporation, *J. Hydrol.*, 593, 125916, <http://doi.org/10.1016/j.jhydrol.2020.125916>, 2021.



- 495 Tramontana, G., Jung, M., Schwalm, C. R., Ichii, K., Camps-Valls, G., Ráduly, B., Reichstein, M., Arain, M. A., Cescatti,
A., Kiely, G., Merbold, L., Serrano-Ortiz, P., Sickert, S., Wolf, S., and Papale, D.: Predicting carbon dioxide and energy
fluxes across global FLUXNET sites with regression algorithms, *Biogeosci.*, 13, 4291–4313, <https://doi.org/10.5194/bg-13-4291-2016>, 2016.
- Trenberth, K. E., Fasullo, J. T., and Kiehl, J.: Earth's global energy budget., *Bull. Am. Meteorol. Soc.*, 90, 311–324,
500 <https://doi.org/10.1175/2008BAMS2634.1>, 2009.
- Trenberth, K. E., Smith, L., Qian, T., Dai, A., and Fasullo, J.: Estimates of the global water Budget and its annual cycle
using observational and model data, *J. Hydrometeorol.*, 8, 758–769, <https://doi.org/10.1175/JHM600.1>, 2007.
- Wang, W., Xiao, W., Cao, C., Gao, Z., Hu, Z., Liu, S., Shen, S., Wang, L., Xiao, Q., Xu, J., Yang D., and Lee X.: Temporal
and spatial variations in radiation and energy balance across a large freshwater lake in China, *J. Hydrol.*, 511, 811–824,
505 <https://doi.org/10.1016/j.jhydrol.2014.02.012>, 2014.
- Yang, Y., and Roderick, M. L.: Radiation, surface temperature and evaporation over wet surfaces, *Q. J. R. Meteorol. Soc.*,
145, 1118–1129, <https://doi.org/10.1002/qj.3481>, 2019.
- Zhang, Y., Peña-Arancibia, J. L., McVicar, T. R., Chiew, F. H., Vaze, J., Liu, C., Lu, X., Zheng, H., Wang, Y., and Liu, Y.
Y.: Multi-decadal trends in global terrestrial evapotranspiration and its components, *Sci. Rep.*, 6, 19124,
510 <https://doi.org/10.1038/srep19124>, 2016.
- Zhang, K., Zhu, G., Ma, J., Yang, Y., Shang, S., and Gu, C.: Parameter analysis and estimates for the MODIS
evapotranspiration algorithm and multiscale verification, *Water Resour. Res.*, 55(3), 2211–2231,
<https://doi.org/10.1029/2018wr023485>, 2019.
- Zhou, S., Williams, A. P., Berg, A. M., Cook, B. I., Zhang, Y., Hagemann, S., Lorenz, R., Seneviratne, S. I., and Gentile, P.:
515 Land–atmosphere feedbacks exacerbate concurrent soil drought and atmospheric aridity, *P. Natl. Acad. Sci. USA*, 116,
18848–18853, <https://doi.org/10.1073/pnas.1904955116>, 2019.



Table 1. List of the chosen FLUXNET sites

Site ID	Lon. (°E)	Lat. (°S)	Data period	Site ID	Lon. (°E)	Lat. (°S)	Data period
AU-ASM	133.25	22.28	2010-2014	AU-How	131.15	12.49	2001-2014
AU-Cpr	140.59	34.00	2010-2014	AU-Rig	145.58	36.65	2011-2014
AU-DaP	131.32	14.06	2007-2013	AU-Stp	133.35	17.15	2008-2014
AU-DaS	131.39	14.16	2008-2014	AU-TTE	133.64	22.29	2012-2014
AU-Dry	132.37	15.26	2008-2014	AU-Tum	148.15	35.66	2001-2014
AU-Emr	148.47	23.86	2011-2013	AU-Wac	145.19	37.43	2005-2008
AU-Fog	131.31	12.55	2006-2008	AU-Whr	145.03	36.67	2011-2014
AU-Gin	115.71	31.38	2011-2014	AU-Wom	144.09	37.42	2010-2014



520

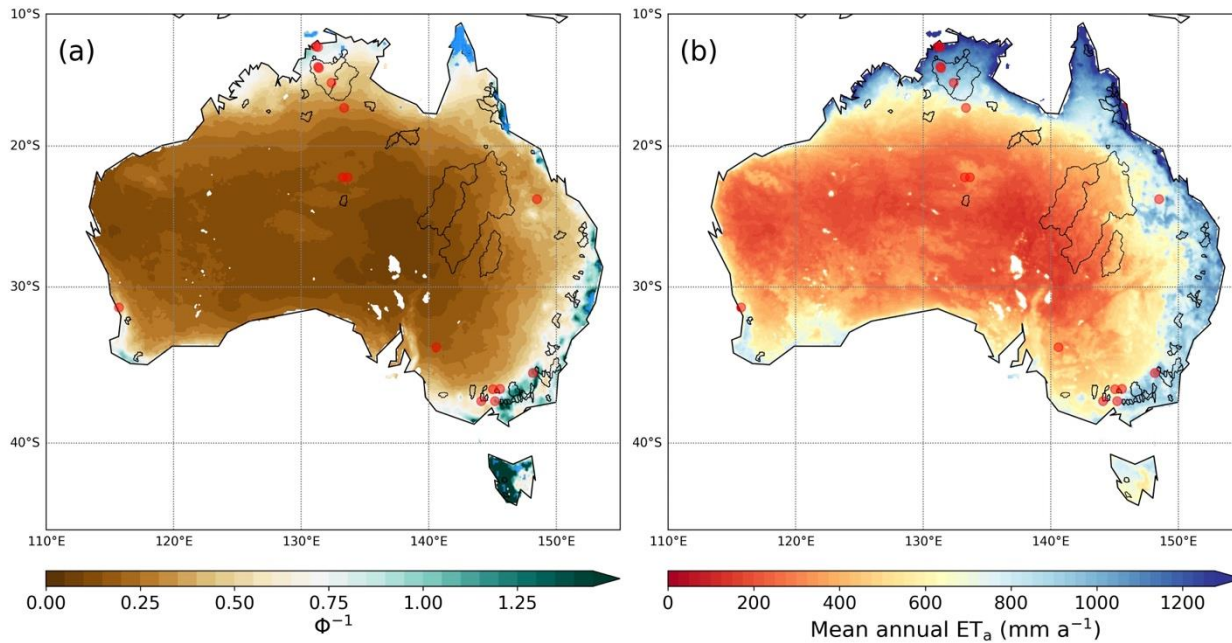


Figure 1: The spatial distributions of (a) wetness index and (b) mean annual ET_a for 1981-2014 predicted by the calibration-free CR. The red circles and the gray polygons are the chosen flux towers and the CAMELS river basins. The blue-colored areas in (a) indicate the wet cells identified by $RH > 90\%$ and $T_{ws} > T_a + 2\text{ }^\circ\text{C}$. CR ET_a was simulated at grid cells where the land fraction was larger than 50%.

525

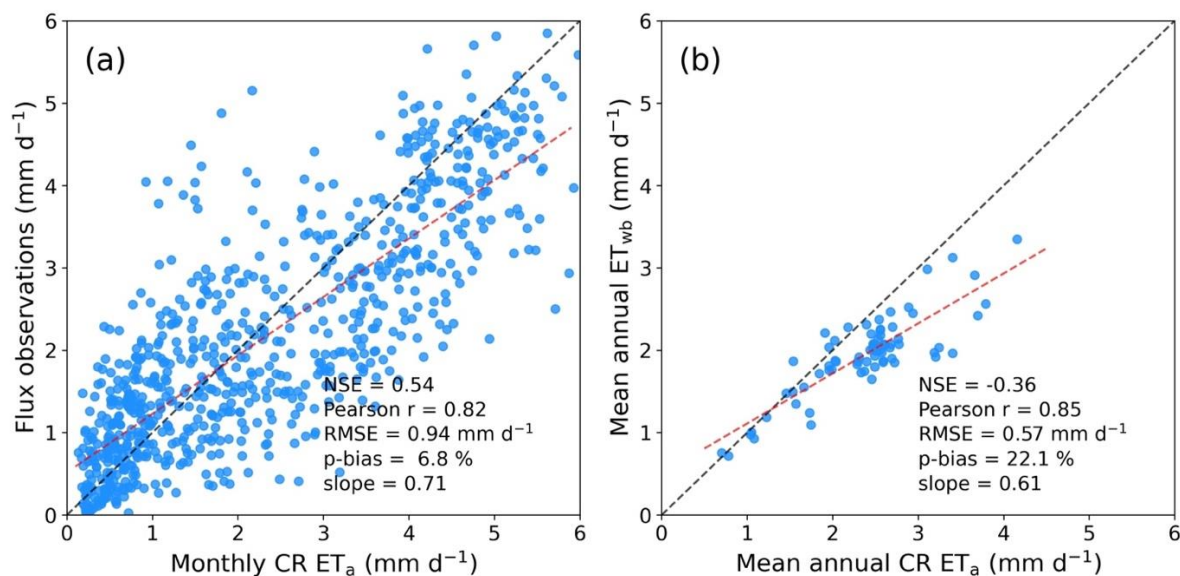
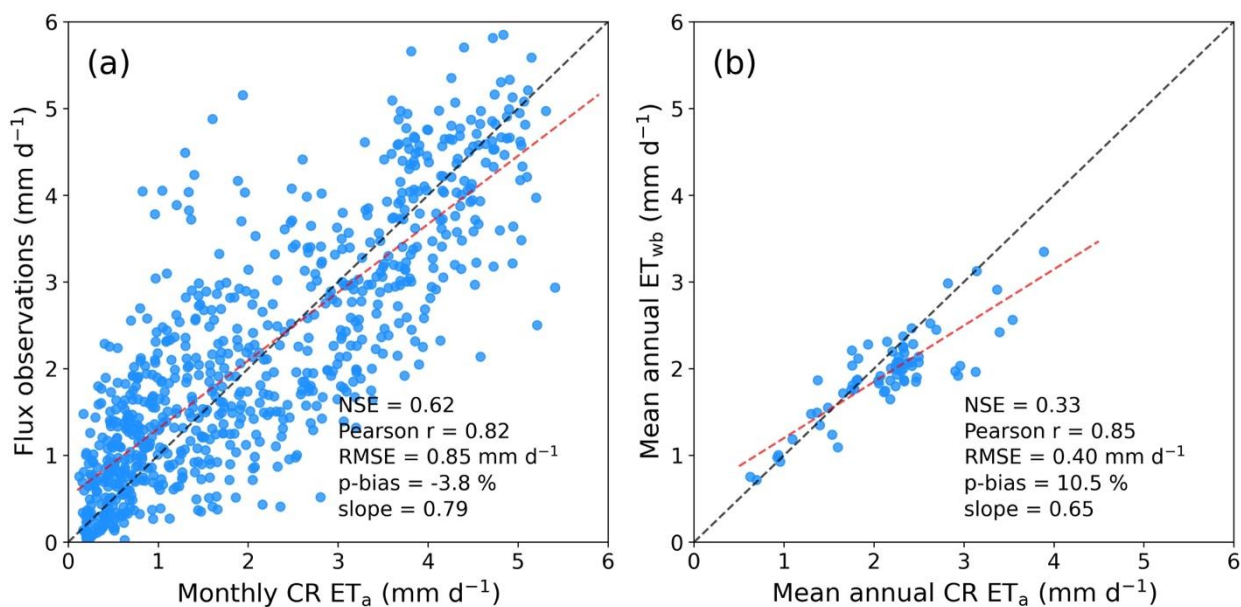
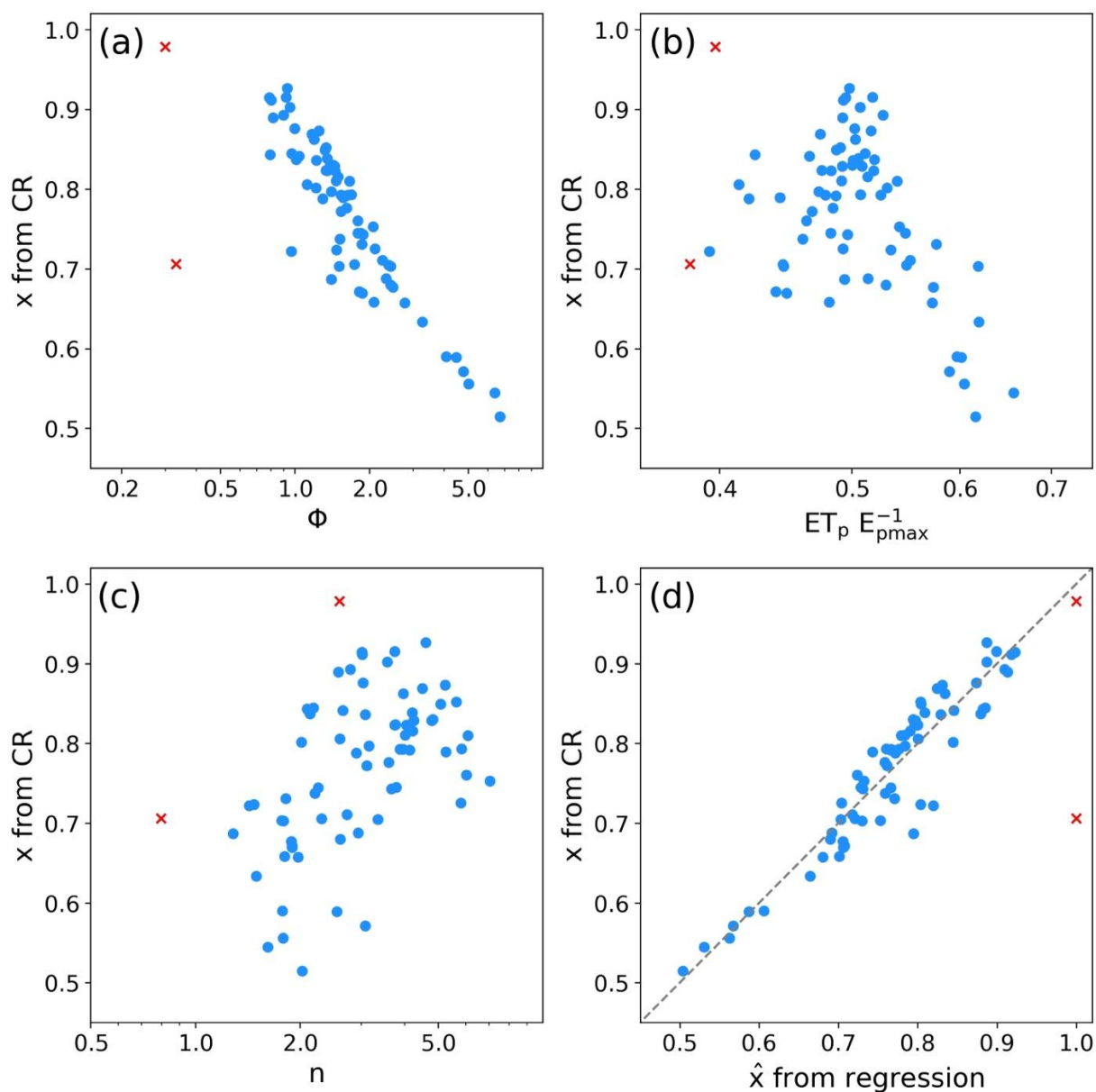


Figure 2: The 1:1 comparison between the calibration-free CR ET_a estimates against (a) the monthly FLUXNET2015 observations and (b) the mean annual ET_{wb} at 71 CAMELS for 1981-2014 predicted by the calibration-free CR.

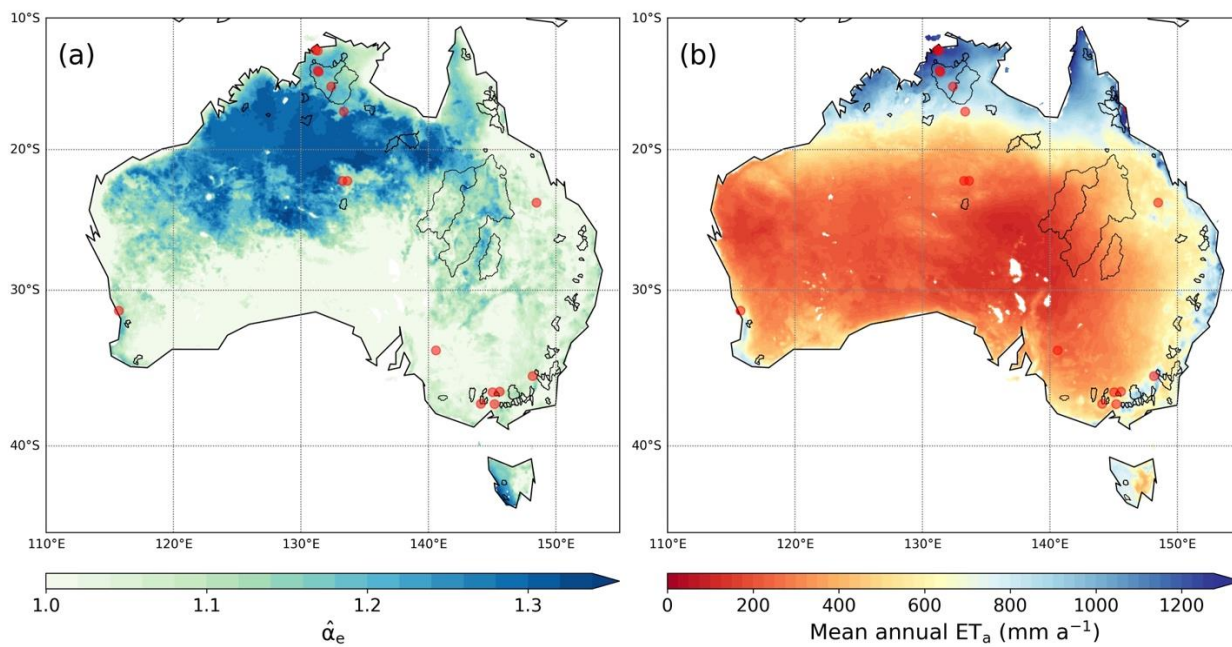


530

Figure 3: As in Figure 2, but with $\alpha_e = 1.10$.



535 **Figure 4:** The scatter plots between the x from the CR with ET_{wb} and corresponding (a) Φ , (b) ET_p/E_{pmax} , and (c) n values, and (d) the 1:1 plot between the x and the predicted \hat{x} by Eq. (15). The red x symbols are the outliers excluded from the correlation and the regression analyses.



540 **Figure 5: The distributions of (a) $\hat{\alpha}_e$ values upscaled by the Budyko framework, and (b) the mean annual ET_a predicted by the CR method with $\hat{\alpha}_e$.**

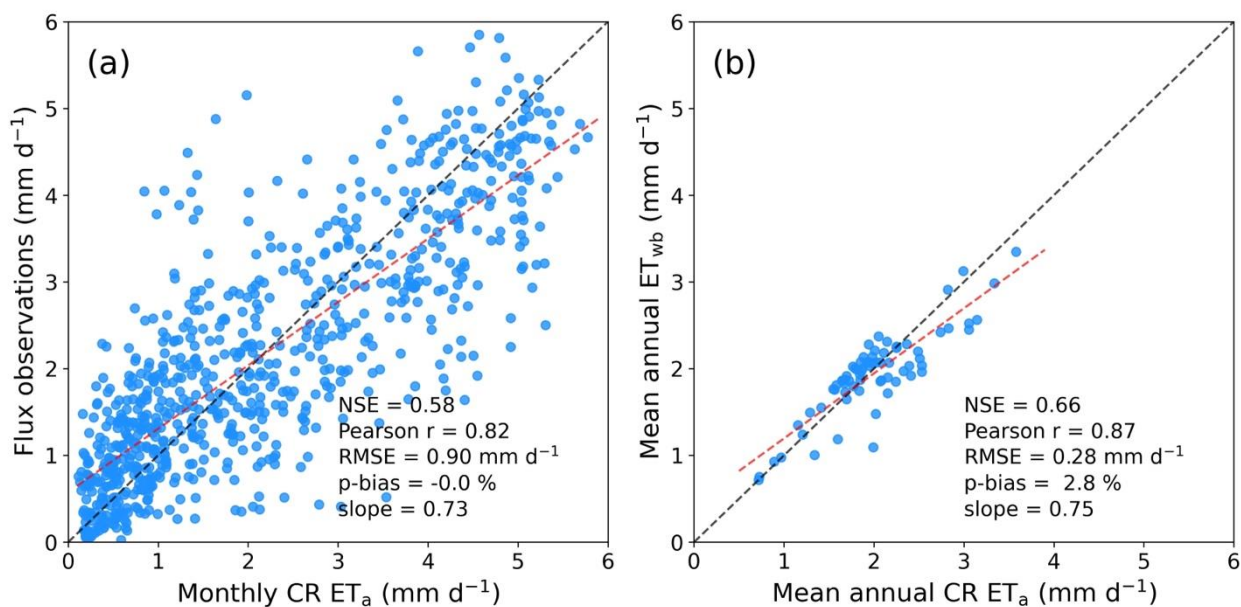


Figure 6: As in Figure 2, but with $\hat{\alpha}_e$ varying across the land surfaces.

545

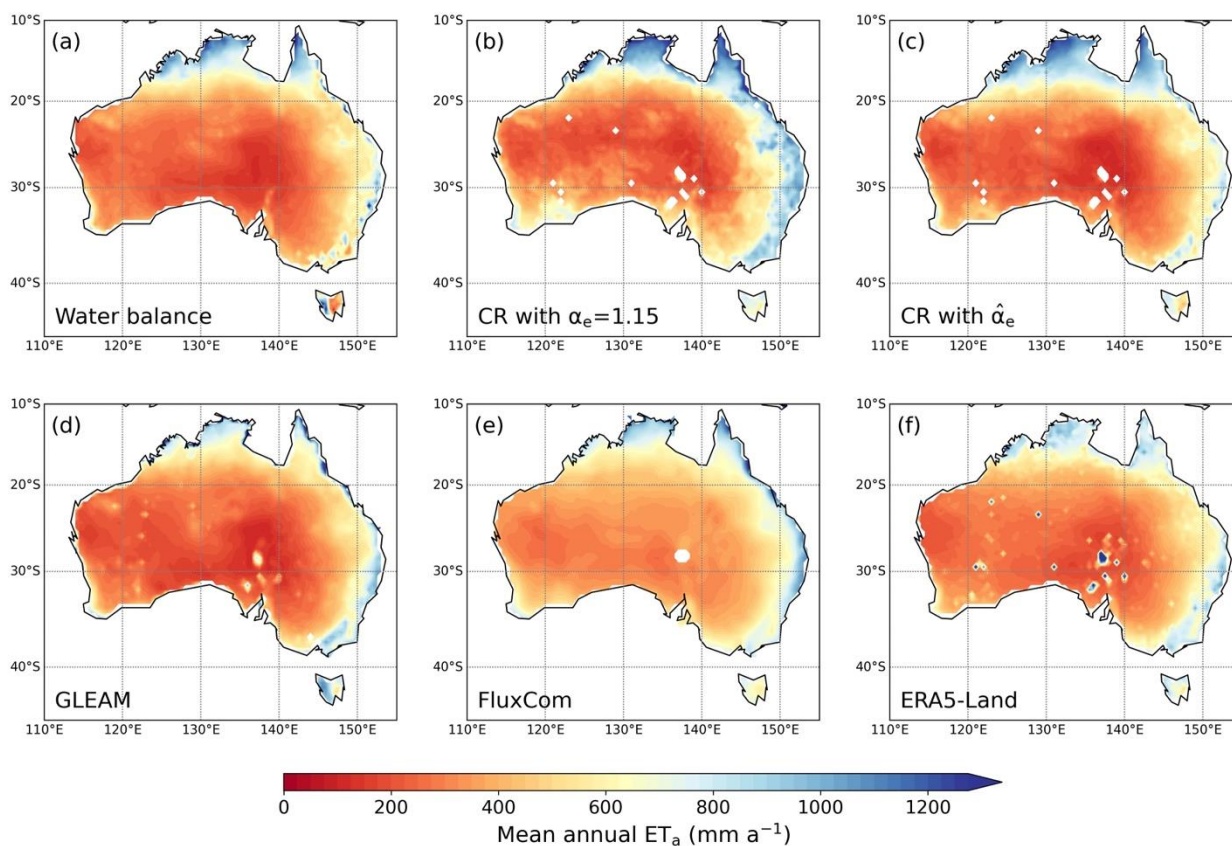
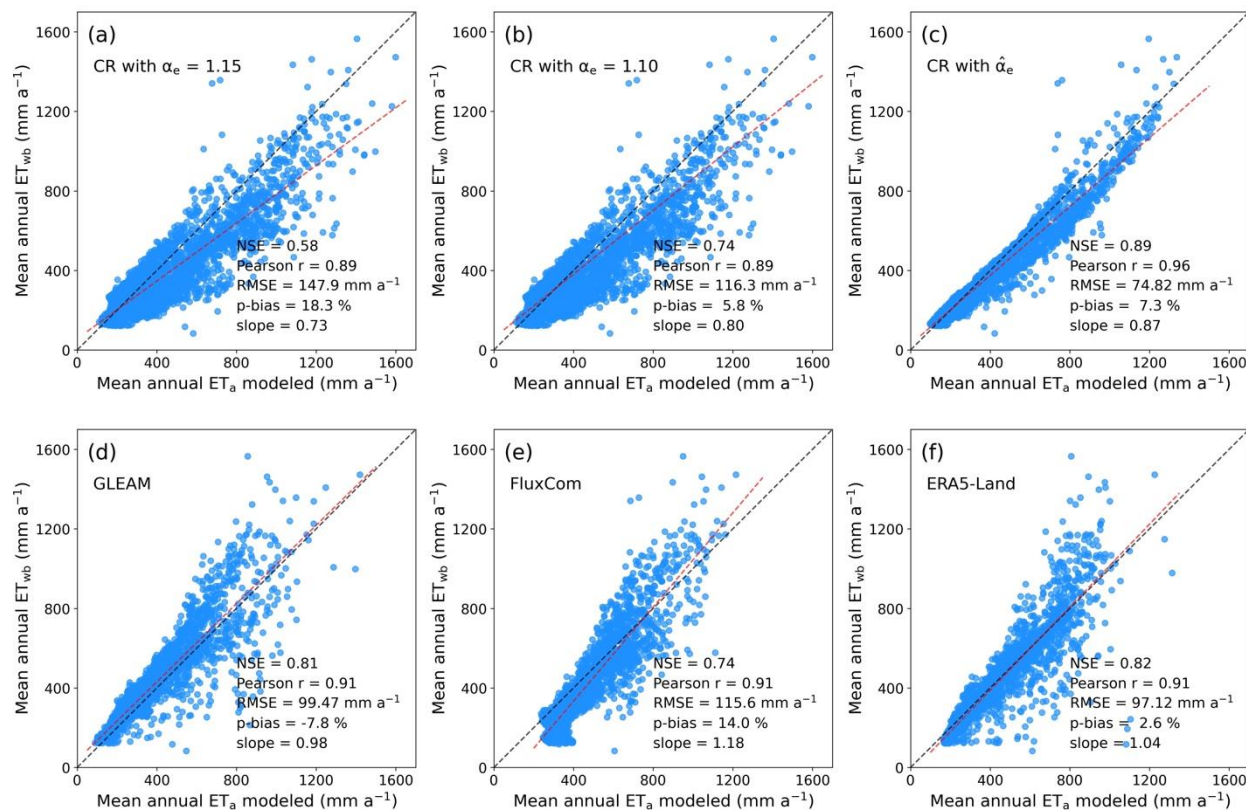


Figure 7: The distributions of (a) the mean annual water-balance ET_{wb} for 1981-2016 and the predictions by (b) CR with $\alpha_e = 1.10$, (c) CR with $\hat{\alpha}_e$, (d) GLEAM, (e) FluxCom, and (f) ERA5-Land.



550

Figure 8: Scatter plots between the mean annual ET_{wb} for 1981-2016 at $0.5^\circ \times 0.5^\circ$ and the predictions by (a) CR with $\alpha_e = 1.15$, (b) CR with $\alpha_e = 1.10$, (c) CR with $\hat{\alpha}_e$, (d) GLEAM, (e) FluxCom, and (f) ERA5-Land.